Am J Transl Res 2020;12(12):7812-7825
www.ajtr.org /ISSN:1943-8141/AJTR0118389

Original Article

Polydopamine coating with static magnetic field promotes the osteogenic differentiation of human bone-derived mesenchymal stem cells on three-dimensional printed porous titanium scaffolds by upregulation of the BMP-Smads signaling pathway

Lingpeng Kong*, Yong Han*, Qingsen Lu, Dongsheng Zhou, Bomin Wang, Dawei Wang, Wupeng Zhang, Hao Xiang, Mingzhen Li, Fu Wang

*Department of Orthopaedics, Shandong Provincial Hospital Affiliated to Shandong First Medical University, No. 324, Jingwu Road, Jinan 250021, Shandong, P. R. China. *Equal contributors.*

Received July 17, 2020; Accepted October 28, 2020; Epub December 15, 2020; Published December 30, 2020

Abstract: Bone regeneration has always been a hot topic for orthopedic surgeons. The role of polydopamine coating in promoting bone regeneration has attracted much attention. Static magnetic field (SMF) is considered an effective and noninvasive treatment for enhancing bone regeneration. However, the effect of polydopamine combined with SMF on bone regeneration on scaffolds is not clear. The aim of this study was to investigate the effects and potential mechanism of polydopamine coating combined with SMF on bone regeneration in three-dimensional printed scaffolds. The polydopamine coating (pTi group) was applied onto porous Ti6Al4V scaffolds (Ti group). Surface characterization was performed by scanning electron microscopy. The 100 mT SMF environment (pTi-SMF group) was established to enhance osteogenic differentiation of human bone-derived mesenchymal stem cells (hBMSCs) on polydopamine coating scaffolds. The cell viability and proliferation were significantly enhanced in the SMF environment (pTi-SMF *vs.* Ti: P=0.005). Improved morphology (pTi-SMF *vs.* pTi: P=0.024, pTi-SMF *vs.* Ti: P=0.001) and adhesion (Ti: $\bar{x}\pm s$=1.585±0.324; pTi: $\bar{x}\pm s$=2.164±0.314; pTi-SMF: $\bar{x}\pm s$=4.634±0.247, P<0.001) of hBMSCs were observed in the pTi-SMF group. The high expression of osteogenesis-related RNA and protein (ALP: Ti, $\bar{x}\pm s$=1.249±0.218; pTi, $\bar{x}\pm s$=2.503±0.209; pTi-SMF, $\bar{x}\pm s$=2.810±0.246. OCN: Ti, $\bar{x}\pm s$=1.483±0.304; pTi, $\bar{x}\pm s$=3.636±0.322; pTi-SMF, $\bar{x}\pm s$=4.641±0.278. Runx2: Ti, $\bar{x}\pm s$=1.372±0.227; pTi, $\bar{x}\pm s$=3.054±0.229; pTi-SMF, $\bar{x}\pm s$=3.914±0.253) was found in the pTi-SMF group (pTi-SMF *vs.* Ti: P<0.001). Proteomics was applied to explore the osteogenic mechanism of polydopamine coating combined with SMF. A total of 147 different proteins were identified between the pTi-SMF and Ti group. The osteogenic effect might be associated with the BMP-Smads signaling pathway (pTi-SMF *vs.* Ti: BMPR1A, P=0.001; BMPR2, P<0.001; Smad4, P=0.001; Smad1/5/8, P=0.008). In conclusion, the osteogenic differentiation of hBMSCs on polydopamine coating scaffolds could be enhanced by SMF stimulation by upregulation of the BMP-Smads signaling pathway.

Keywords: Osteogenesis, polydopamine, static magnetic field, three-dimensional printing, titanium alloy scaffold

Introduction

Bone nonunion and bone defects are intractable problems in orthopedic clinical treatment at present. Nonunion is usually defined as a fracture that does not heal after 9 months of treatment and shows no further signs of healing within 3 months. Nonunion defects not only result in limited limbs but also have severe negative effects on daily life. So far, surgery has made tremendous strides, and autologous and allogeneic bone has been widely used to repair bone nonunion or defects caused by trauma, tumor resection or congenital diseases [1]. However, autogenous and allogeneic bone grafts are limited by a shortage of supplies, the potential risk of donor lesions and disease transmission [1, 2]. In tissue engineering, scaffolds play an important role in supporting cell attachment, proliferation and differentiation.

For bone tissue engineering, scaffolds must have the characteristics of load-bearing and cell adhesion to promoting bone regeneration [3]. The ideal scaffold can restore mechanical function and support good interface interaction [4, 5].

The application of three-dimensional printed (3DP) technology is a new direction in the research of tissue engineering scaffold materials [6]. Given their advantages of low corrosion, low stiffness (similar to cortical bone) and good biocompatibility, 3DP porous titanium scaffolds are one of the most promising medical substitutes for treatment bone defects in clinical practice, but their current application is limited by poor biological activity [7, 8]. To overcome this defect, various surface modification and physical stimulation techniques have been explored. Recent studies have shown that in an alkaline environment, the catechin groups of dopamine can simply form a polydopamine layer on the surface of titanium, which plays a crucial role in enhancing the adhesion of bioactive molecules and surface modification of scaffold materials [9]. PDA coatings that improve the surface properties of implants are one of the most beneficial features of a wide range of chemical properties related to bone regeneration [10]. In addition, PDA coating can increase the expression of bone-related genes by stimulating the adhesion and proliferation of primitive cells [11, 12].

With the development of biomagnetic technology, research on the biological effects of magnetic fields has achieved positive results, and basic and clinical research on magnetic therapy in medicine is becoming more extensive. At the cellular level, a static magnetic field (SMF) regulates many cellular behaviors, such as proliferation, cell cycle distribution, ion channels, metabolic activity, morphology, gene expression, apoptosis and so on [13]. In addition, some SMFs also promote osteoblast healing and bone formation *in vitro* and *in vivo* [14]. These studies suggest that SMF could be used as a physiotherapy for the maintenance of bone health and the treatment of bone diseases [15]. Given the cost, adverse effects and potential risks associated with medical or surgical treatment, magnetic therapy is noninvasive and may be considered an effective treatment [16, 17]. SMF does not provide any energy to stimulate tissue, so there is no thermal or electrical hazard to bone tissue. From this point of view, SMF is safe and suitable for long-term use. Therefore, SMF is noninvasive, safe and easy to use and has a broad application prospects in the treatment of many bone diseases [18].

Although researchers have done some research on polydopamine or SMF in bone diseases, research on polydopamine coating combined with SMF to promote bone regeneration of human bone-derived mesenchymal stem cells (hBMSCs) on 3DP scaffolds has not been reported. In this work, we investigated the effect of polydopamine with SMF on the bone regeneration of 3DP Ti6Al4V scaffolds and preliminarily explored the mechanism of bone regeneration by proteomic analysis.

Materials and methods

3D printed porous titanium alloy scaffold

The 3DP porous titanium bracket scaffold is made of Ti6Al4V and has the following geometry: diameter 5 mm, height 1 mm, strut width 200 μm, aperture 600 μm and porosity over 85%. Selective laser melting (Concept Laser, Lichtenfels, Germany) and postproduction heat treatment were used to fabricate the structure. Prior to use, all scaffolds were validated with computed tomography (CT) (Inspisio SMX-90CT Plus; Shimadzu, Kyoto, Japan).

Preparation of pTi

The 3DP scaffolds were washed by ultrasound in acetone, ethanol and deionized water (dH_2O) 3 times and then used. A 3D printed porous titanium scaffold was immersed in a dopamine solution (2 mg/mL, 10 mM Tris-HCl buffer, pH=8.5; Sigma-Aldrich, MO, USA) at room temperature. The polydopamine coating 3D printed porous titanium scaffold was washed three times by ultrasound in deionized water (dH_2O) to remove the unattached dopamine molecules and then dried in nitrogen. The surface morphology of the samples was visualized by scanning electron microscope (JSM-6700F, Jeol, Tokyo, Japan).

Cell culture and proliferation

The hBMSCs was purchased from Shanghai Zhong Qiao Xin Zhou Biotechology Co., Ltd. (Shanghai, China) and incubated in basic cul-

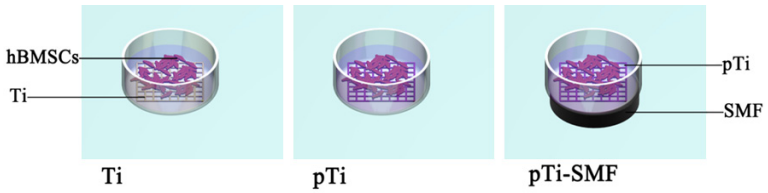

Figure 1. Diagram of experimental grouping. hBMSCs were cultured on 3D printed porous titanium scaffolds in the Ti group, and the hBMSCs were modified with polydopamine coating in the pTi group, and permanent magnets were assembled in the pTi-SMF group under a cell culture dish to realize SMF environment.

ture medium (Sciencell, USA) supplemented with 10% fetal bovine serum (Gibco, USA), 1% penicillin-streptomycin and glutamine (Roche, Switzerland) in an incubator (Sanyo, Japan) with 5% CO_2 at 37°C and saturated humidity. After growing and reproducing to approximately 80% confluency, hBMSCs were dissolved with 0.25% trypsin (Dalian Meilun Biotechology Co., Ltd., Dalian, China) for further use. The medium was changed once every 2-3 days. The third-fifth generations of cells were used in the experiment. hBMSCs were seeded onto the surfaces of scaffolds in 6-well culture plates for follow-up experiments. To investigate the effect of polydopamine coating with SMF, the 3DP scaffolds group (Ti group) was used as the control group, while polydopamine coated 3DP scaffolds with or without SMF (pTi-SMF group or pTi group) were used as experimental groups.

To build the SMF environment, a Nd2Fe14B magnet (1 mm thick, 15 m in diameter; Qingdao Qiangsheng Magnets, Shandong, China, **Figure 1**) was assembled under the cell culture plate. The required effective SMF intensity was achieved by adjusting the distance between the magnet and the cells. Measurement of SMF values was performed using a digital Teslameter (HT20; Hengtong, Shanghai, China). A previous study reported that 100 mT SMF had a relatively good effect on bone regeneration [19]. Therefore, we controlled the SMF value at 100 mT and stimulated the hBMSCs in a dynamic manner at 12-hour SMF exposure intervals. In the process of cell incubation, the SMF-treated group and untreated group were completely separated.

Cell activity and proliferation

The cytotoxicity was determined by the LIVE/DEAD reagent kit (Invitrogen). After the cells were inoculated and incubated for 3 days, samples were taken from the 6-well plate and washed with PBS 3 times. One milliliter of reagent was then immediately added to each sample and incubated in darkness at 37°C for 30 minutes. All samples were then observed with a Leica TCS SP8X confocal laser scanning microscope (Leica Microsystems GmbH, Wetzlar, Germany). Immunofluorescence imaging was performed at six different sites for each sample (n=3) in the region of interest. The living cell ratio was calculated using IMAGEJ software (NIH, Bethesda, MD, USA).

The cell proliferation rate was measured by a cell counting kit-8 (CCK-8). hBMSCs were incubated at 37°C for 60 minutes in a 10:1 ratio of fresh culture medium and CCK-8 (Sigma-Aldrich, MO, USA) after 1, 4 and 7 days. The absorbance of supernatant was measured by microplate reader (Bio-Rad, Hercules, CA) at 450 nm.

Cell morphology and adhesion

F-actin, vinculin and 4',6-diamidino-2-phenylindole (DAPI) staining were used to observe the cell morphology and adhesion. hBMSCs were cultured for 3 days in osteoblastic differentiation medium (HUXMA-90011; Cyagen Biosciences, Santa Clara, CA, USA) containing osteoblastic differentiation fetal bovine serum, penicillin-streptomycin, dexamethasone, ascorbic acid, glutamine, and glycerophosphate. The cells were immobilized in 4% polyformaldehyde (Sigma-Aldrich, MO, USA), ventilated for 15 minutes using 0.5% Triton X-100 (Sigma-Aldrich, Mo, USA), and sealed for 1 hour in 1% bovine serum albumin (Gibco, USA) at room temperature. At 4°C, the cells were incubated overnight in primary antibodies against vinculin (1:250; Abcam, Cambridge, MA, USA). Cells were incubated for 1 hour with FITC-conjugated goat anti-rabbit secondary antibodies (1:5000; Abcam) at room temperature and in darkness. F-actin with TRITC Phalloidin (Yeasen, Shanghai, China) was applied for 30 minutes at room temperature in the dark, and cell nuclei were counterstained with DAPI (Thermo Fisher Scientific) for 3 minutes. A fluorescence microscope (Leica TCS SP8X, Germany) was used to capture the images. The total cell/nucleus

Table 1. Real-time PCR primers

Gene	Forward primer sequences (5'-3')	Reverse primer sequences (5'-3')
ALP	ACGAGCTGAACAGGAACAACGT	CACCAGCAAGAAGAAGCCTTTG
Col-1	GACGAAGACATCCCACCAAT	AGATCACGTCATCGCACAAC
RUNX2	CGCATTCCTCATCCCAGTAT	GCCTGGGGTCTGTAATCTGA
GAPDH	CGACAGTCAGCCGCATCTT	CCAATACGACCAAATCCGTTG

(C/N) area ratio and vinculin fluorescence intensity were calculated by IMAGEJ software (National Institutes of Health (NIH), Bethesda, MD, USA).

qPCR

The hBMSCs were seeded onto the samples and incubated in an osteoblastic differentiation medium (HUXMA-90021; Cyagen Biosciences) for 14 days. The expression levels of ALP, Collagen type I (Col-1), osteocalcin (OCN) and runt-related transcription factor-2 (RUNX2) in hBMSCs were determined by quantitative PCR. All mRNA was extracted with TRIzol reagent (Invitrogen, Carlsbad, CA, USA), then reverse transcribed into cDNA by a cDNA Synthesis Kit (GeneDireX, Taipei, Taiwan). The primer sequence of each gene is shown in **Table 1**.

The SYBR FAST qPCR Kit (Invitrogen, Carlsbad, CA, USA) was used to carry out RT-PCR reactions in a StepOne Plus RT-PCR instrument (Applied Biosystems, Foster City, CA, USA). GAPDH was used as a housekeeping gene, and the osteogenetic expression level was determined by the $2^{-\Delta\Delta CT}$ method.

Proteomic analysis

The proteomic differences between Ti and pTi-SMF groups were detected by unlabeled quantitative analysis and protein identification. In short, the total proteins of both groups were purified and digested by filtration-assisted sample preparation. The protein was extracted from cells in 4% SDS (Yeasen, Shanghai, China) and incubated at room temperature for 30 minutes. The pyrolysate was ultrasonically treated and boiled at 95°C for 5 minutes. All samples were digested in a strainer with trypsin all night. The digested samples were purified and desalted on C18 Solid Phase Extraction Columns (Hawach scientific; Xian, Shanxi, China) using a Qiavac 24 Plus vacuum manifold (Qiagen, Germantown, MD, USA). These proteins were studied using a Q-Exactive mass spectrometer (Thermo Fisher Scientific) and Easy-nLC1000 (Thermo Fisher Scientific). The peak areas of ion chromatography and liquid chromatography were compared by tandem mass spectrometry to calculate the relative expression levels of the identified proteins. The original files were analyzed by MaxQuant Software (v.1.5.3.8; Max Planck Institute of Biochemistry, Planegg, Germany). Gene ontology term enrichment and Kyoto Encyclopedia of Genes and Genomes (KEGG) were used for bioinformatics analysis.

Extracellular matrix mineralization

Alizarin red staining (ARS) and alkaline phosphatase (ALP) activity were used to evaluate extracellular matrix (ECM) mineralization. An indirect method was used to observe ARS. The cells on the culture plate were fixed with 4% formaldehyde for 30 minutes and stained with ARS for 5 minutes. Visualization was performed using an optical microscope. The combined dye was washed with 10% acetic acid (Nanjing Reagent, Jiangsu, China), then centrifuged and neutralized with 10% ammonium hydroxide (Nanjing Reagent). A microplate reader was used for quantitative analysis at the optical density of 405 nm. After 7 and 14 days of culture on osteogenic differentiation medium, the activity of ALP was evaluated using the ALP Kit (Shanghai Fusheng Industrial Co., Ltd., Shanghai, China). hBMSCs were lysed at 4°C for 2 hours using 0.1% Triton X-100 and Tris-HC (10 mM, pH 7.4). The cells were incubated at 37°C for 15 minutes after p-nitrophenyl phosphate was mixed with the lysate. A microplate reader was used for quantitative analysis at the optical density of 405 nm. The activity of standardized ALP was determined by a Bicinchoninic Acid Kit (AppliChem, Omaha, Nebraska, USA).

Western blotting

The expression levels of Col-1, ALP and RUNX2 were assessed by western blotting. hBMSCs were cultured in osteoblast differentiation medium for 14 days and then lysed with lysis buffer (Yeasen, Shanghai, China). Total protein levels were quantified using a Bicinchoninic Acid Kit (applicchem, Omaha, Nebraska, USA). SDS-PAGE was used to separate the same

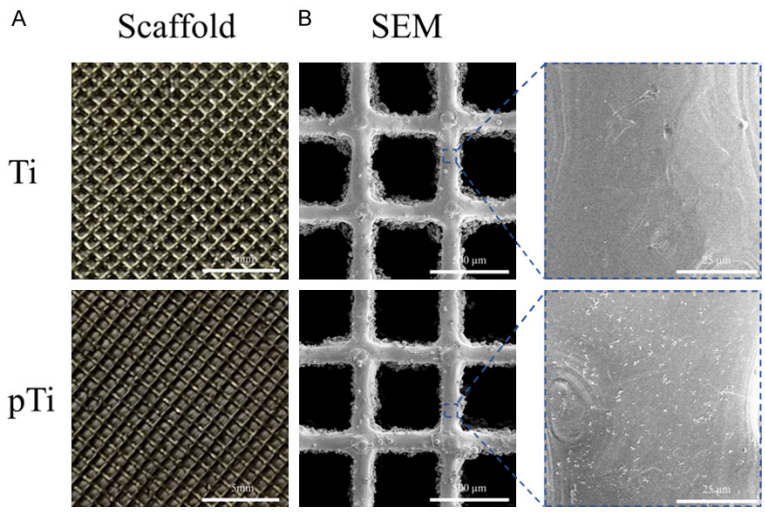

Figure 2. A. Surface morphology of a 3D printed porous titanium scaffold. B. The required scaffoldporosity and Surface roughness are enlarged by SEM to 10 (scale, 500 μm) and 200 (scale, 25 μm). (Ti) SEM image of 3D printed porous titanium scaffoldwithout polydopaminecoating; (pTi) SEM image of 3D printed porous titanium scaffoldwith polydopaminecoating.

amount of protein and transfer it to a PVDF membrane. The membrane was sealed in 5% skimmed milk at room temperature for 1 hour and was mixed with anti-Col-1 (1:1000; Abcam), ALP (1:500; Abcam), and Runx2 (1:1000; Abcam) at 4°C. Horseradish peroxidase-conjugated secondary antibodies (1:2000; Thermo Fisher Scientific) were incubated at room temperature for 60 minutes. GAPDH antibody (1:1000, proteintech™, Wuhan, China) was used as the loading control. Imprinting was detected using an Enhanced Chemilescent Kit (Yeasen, Shanghai, China) and quantified using IMAGEJ software.

Based on the results of proteomics and related proteins in their pathways, western blotting was performed to evaluate specific related proteins, including Bone morphogenetic protein receptors type IA (BMPR1A) (1:1000; Abcam), BMPR2 (1:1000; Abcam), Smad4 (1:1000; Cell Signaling Technology), and pSmad1/5/8 (1:1000; Cell Signaling Technology).

Statistical analysis

The experiment was conducted three times. SPSS Statistics 23.0 (SPSS, Inc., Al Monk, NY, USA) was used for statistical analysis. The results were expressed as the mean standard deviation. The differences among the three groups were investigated by single factor analysis of variance and an independent sample *t-test*. The difference was statistically significant with $P< 0.05$.

Result

Scaffold characterization

The 3DP scaffolds showed uniform porous structure with metallic luster from a macroscopic view (**Figure 2**). The 3D printed rough surface with Ti-6Al4V particles was observed by SEM. The polydopamine-coated scaffolds presented a dark surface without metallic luster from a macroscopic view compared to uncoated scaffolds. The Ti6Al4V particles were also observed by SEM. In addition, irregular particulate matter was attached to the surface of polydopamine-coated scaffolds in the high-power field.

Cell activity and cell proliferation

After 1, 4 and 7 days of cell culture, a LIVE/DEAD Viability/Cytotoxicity Assay Kit was used to determine the cell availability of hBMSCs in different groups. Living and dead cells are shown in green and red fluorescence, respectively, and the results are shown in **Figure 3A**. The percentage of living cells in the pTi-SMF group was significantly increased, and the results were statistically significant (P=0.034, **Figure 3B**). The proliferation of hBMSCs was assessed by CCK-8 kit on days 1, 4 and 7 of cell culture. The number of cells in each group increased continuously until 7 days, and we found that there was greater cell proliferation in the pTi-SMF group than in the Ti group (P=0.005, **Figure 3C**). These results indicate that polydopamine coating with SMF can enhance the cell viability and proliferation of hBMSCs in 3DP scaffolds.

Cell morphology and adhesion

F-actin, vinculin and DAPI were used to observe the cell morphology and cell adhesion. Fluorescence of F-actin (red), vinculin (green) and nuclei (blue) showed that the pTi-SMF group had better cell morphology (**Figure 4A**) than the Ti group. The hBMSCs in the Ti group were bipo-

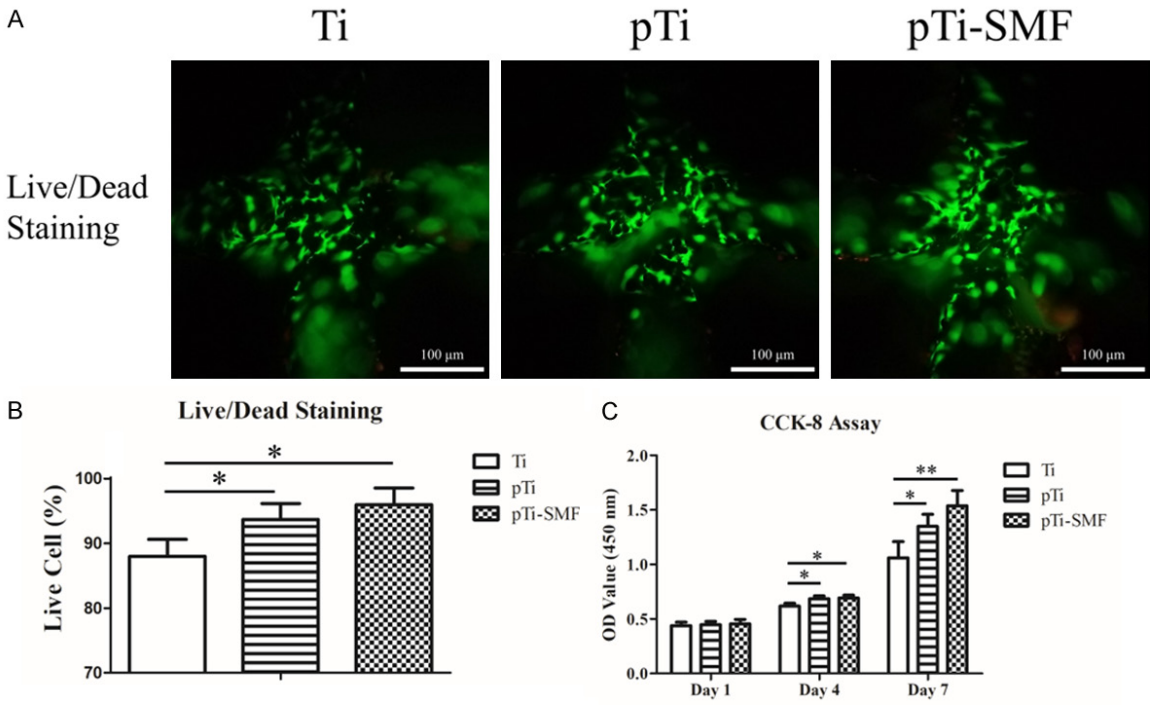

Figure 3. Cell viability and proliferation were measured with Live/Dead and CCK-8, respectively. A. 2.5*10^5 cells/ml hBMSCs were stained with a Live/Dead Viability/Cytotoxicity Assay Kit after 7 days. The ratio of Live/Dead of hBMSCs cultured in Ti group, PTi group and pTi-SMF group was 100 M. The living cells and the dead cells showed green and red fluorescence respectively. B. Quantitative results of a live/dead analysis performed through the IMAGEJ software. C. The proliferation of hBMSCs was quantitatively analyzed by CCK-8 after 1, 4 and 7 days of culture. The experiment was repeated 3 times. Six images were used for analysis. *P<0.05, **P<0.01 vs. Ti group.

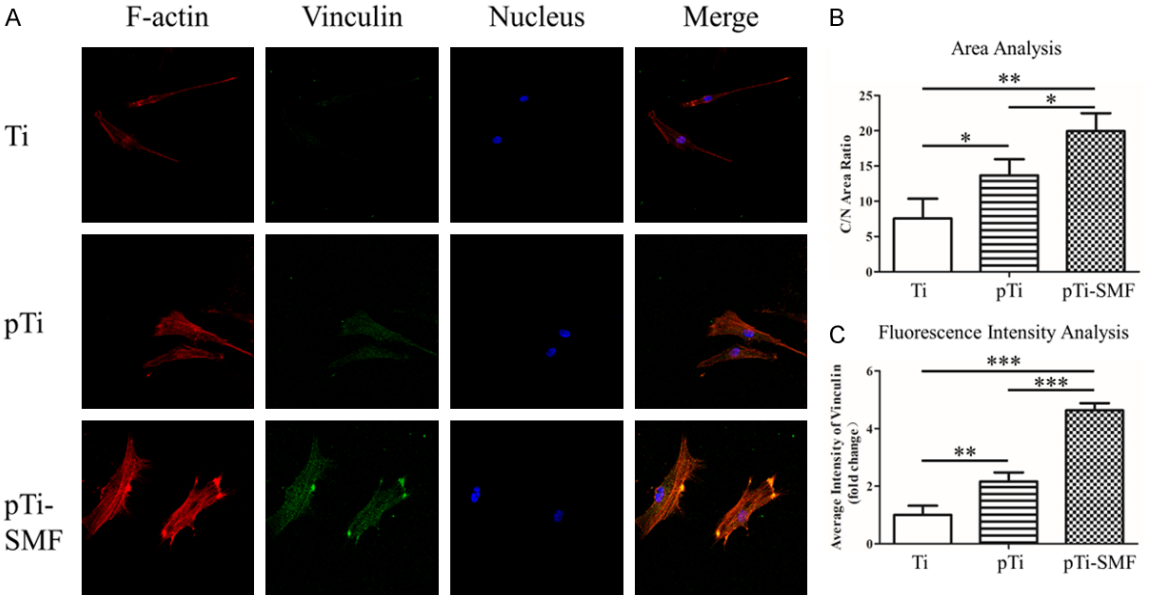

Figure 4. Cell morphology and adhesion determined by F-actin and Vinculin staining. A. After 14 days of culture (2.5*10^5 cells/ml), the hBMSCs adhered to the porous titanium scaffold were stained with F-actin (red), Vinculin (green) and nucleus (blue), and observed with microscope (scale 10 μm). B. A quantitative result of the area ratio of the whole cell to the nucleus (C/N Area Ratio). C. Quantitative results of Vinculin fluorescence intensity of hBMSCs. The experiment was repeated three times. Six images were used for analysis. *P<0.05, **P<0.01, ***P<0.001.

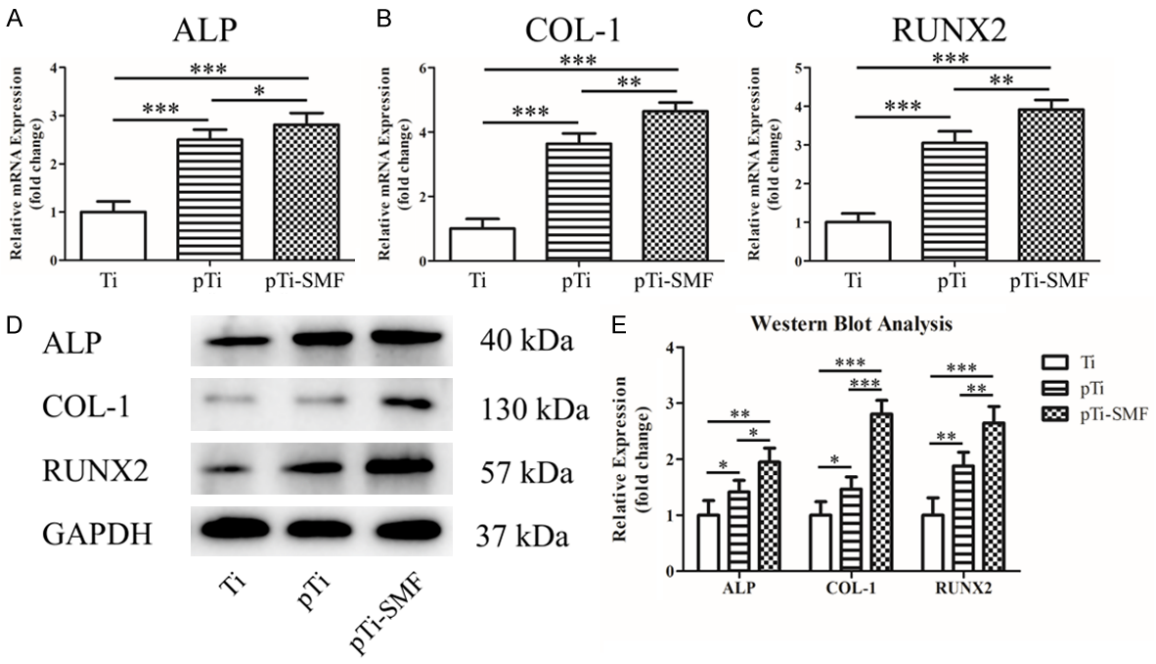

Figure 5. Real-time PCR and western blot were used to detect the expression of osteogenic markers. (A-C) The expression of osteogenic mRNA of ALP (A), col-1 (B) and Runx2 (C) in human bone marrow was detected by real-time quantitative PCR after cultured for 14 days. (D) The protein levels of ALP, Col-1, Runx2 and GAPDH 2.5*10^5 cells/ml were detected by western blot after 14 days. (E) Western blots quantitative analysis for each group. The experiment was repeated three times. *P<0.05, **P<0.01, ***P<0.001.

lar, flat and had no obvious pseudopodia. With the aid of polydopamine, cell polarity increased, and cell pseudopodia were easily found. After exposure to SMF, hBMSCs were multipolar and well-shaped, with obvious actin stress fibers and pseudopodia. SMF could improve the morphology of hBMSCs in polydopamine-coated scaffolds.

For quantitative analysis of cell morphology, we calculated the C:N ratio (total cell area: nucleus area) of each group of cells using IMAGEJ software. The statistical results in **Figure 4B** (P=0.024, P=0.001) show that hBMSCs from the pTi-SMF group have a higher C/N ratio than those of the pTi and Ti groups, and the pTi group has a higher C/N ratio than the Ti group. In addition, the fluorescence intensity of vinculin in pTi-SMF cells increased significantly, and the difference was statistically significant (Ti: $\bar{x}$ ±s=1.585±0.324; pTi: $\bar{x}$±s=2.164±0.314; pTi-SMF: $\bar{x}$±s=4.634±0.247, P<0.001, **Figure 4C**). The results showed that polydopamine coating combined with SMF could improve the morphology of hBMSCs and increase cell adhesion on scaffolds.

Osteogenic differentiation

Real-time PCR and western blotting were used to directly assess the mRNA and protein expression levels of osteogenesis, respectively. The mRNA expression of ALP, OCN and Runx2 was detected by real-time RT-PCR after 14 days of hBMSC induction culture. As shown in **Figure 5A-C**, the mRNA expression levels of ALP (Ti: $\bar{x}$±s=1.249±0.218; pTi: $\bar{x}$±s=2.503±0.209; pTi-SMF: $\bar{x}$±s=2.810±0.246), OCN (Ti: $\bar{x}$±s=1.483±0.304; pTi: $\bar{x}$±s=3.636±0.322; pTi-SMF: $\bar{x}$±s=4.641±0.278) and Runx2 (Ti: $\bar{x}$±s=1.372±0.227; pTi: $\bar{x}$±s=3.054±0.229; pTi-SMF: $\bar{x}$±s=3.914±0.253) in the pTi-SMF group were higher than those in the Ti group (P< 0.001). Accordingly, the protein expression levels of Col-1, ALP, and Runx2 were significantly increased at day 14 in pTi-SMF compared with the other group (**Figure 5D**). Additionally, the difference was statistically significant (**Figure 5E**).

ARS staining and ALP activity can reflect the degree of ECM mineralization to evaluate the state of osteogenic differentiation. As shown in **Figure 6A**, ARS staining shows that polydopa-

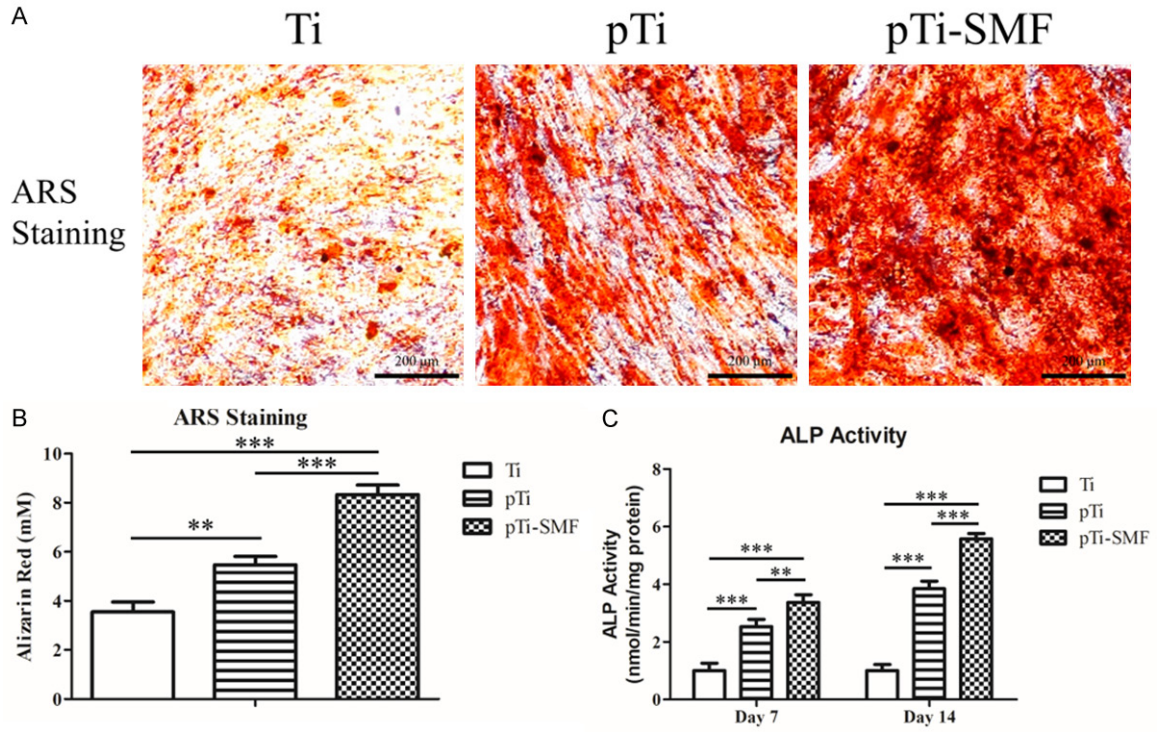

Figure 6. The ARS staining and ALP activity can be used to evaluate ECM calcification. The hBMSCs were cultured on the plates around the titanium scaffolds for 14 days and stained with ARS 2.5*10^5 cells/ml. ARS staining (scale, 200 μm) (A) and Quantitative analysis (B) in Ti, pTi and SMF-pTi groups were performed. ALP activity (C) of HBMSC in each group was detected after 7 and 14 days of incubation (2.5~10^5 cells/ML). The experiment was repeated three times. Six images were used for analysis. *P<0.05, **P<0.01, *** P<0.001.

mine coating enhances ECM mineralization, while SMF further promotes ECM mineralization. The quantitative analysis of calcium accumulation in the pTi-SMF group was significantly higher than that in the other two groups (Ti: $\bar{x}$ ±s=3.543±0.411; pTi: $\bar{x}$±s=5.470±0.345; pTi-SMF: $\bar{x}$±s=8.326±0.395, P<0.001, **Figure 6B**). Alkaline phosphatase plays a key role in the mineralization of bone matrix. ALP activity was measured after 7 (Ti: $\bar{x}$±s=1.463±0.265; pTi: $\bar{x}$±s=2.528±0.258; pTi-SMF: $\bar{x}$±s=3.372±0.264) and 14 (Ti: $\bar{x}$±s=1.445±0.219; pTi: $\bar{x}$±s=3.847±0.264; pTi-SMF: $\bar{x}$±s=5.577±0.189) days of hBMSC culture to evaluate the osteogenic differentiation activity of cells on the surface of 3D printed porous titanium scaffold. The quantitative analysis results (**Figure 6C**) show that the ALP activity in the pTi-SMF group is significantly higher than that in the Ti group (P<0.001) and that in the pTi group is higher than that in the Ti group (P<0.001). These results suggest that the SMF can further enhance the osteogenic differentiation of hBMSCs on polydopamine-coated 3DP scaffolds.

Proteomics results

A total of 147 differential proteins were identified between the Ti and pTi-SMF groups with relative multiples that varied >2 (Table S1). Compared with cells in the Ti group, cells in the pTi-SMF group were classified as presenting 77 proteins with increased relative abundance, and decreased relative abundance was observed for 70 proteins.

The pie chart shows the results of the classification of 147 different proteins according to GO term enrichment (**Figure 7**). The most common biologic process functions (**Figure 7A**) were cellular process 29.46%, RNA regulation 23.21%, cell cycle 10.71%, cell division 9.82%, and protein complex biogenesis 8.92%. The cellular component classification (**Figure 7B**) showed that nucleus 37.83%, cytoplasm 33.78%, cellular membrane 22.30% were the most common locations. The proteins were classified as contributing to protein binding 62.72%, RNA binding 14.20%, and cell cycle 9.47% in the molecu-

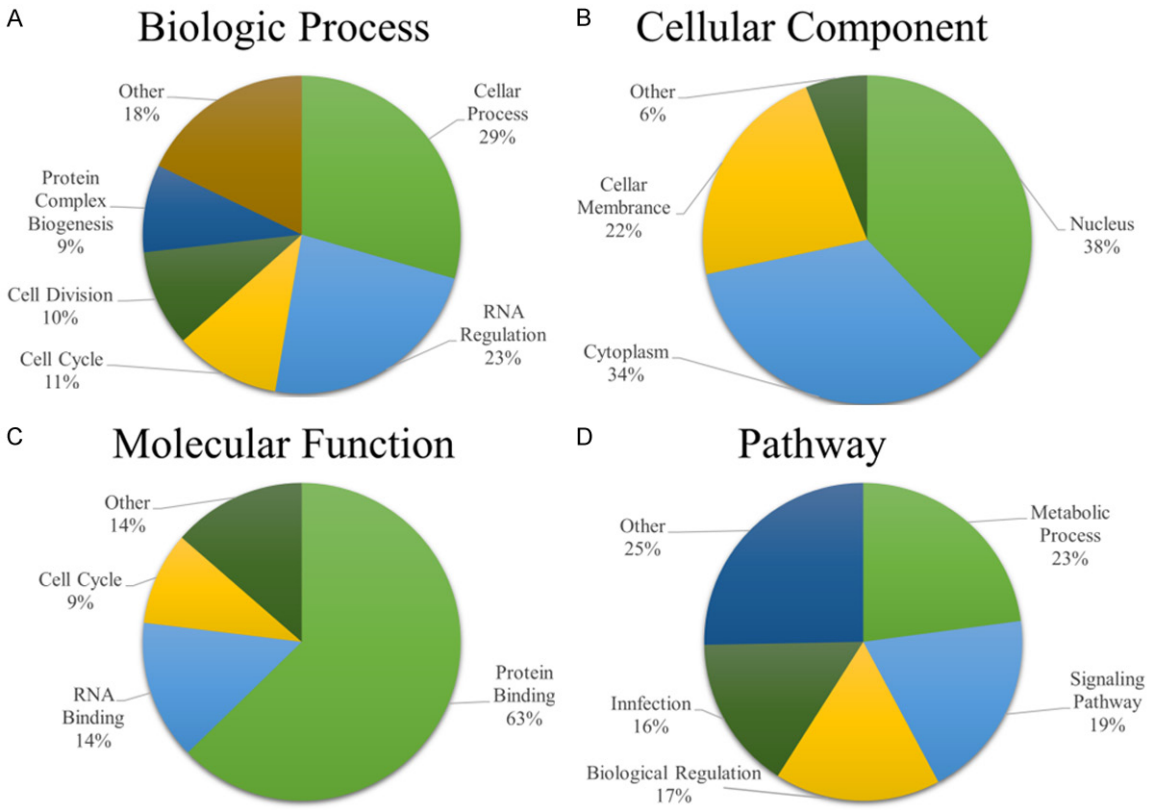

Figure 7. Results of the proteomics analysis. In the GO glossary, the biologic processes (A), cellular components (B), and molecular functions (C) of the classification of 147 different proteins are grouped. (D) Results of KEGG pathway analysis of 147 different proteins. The experiment was repeated three times.

lar function analysis (**Figure 7C**). The KEGG pathway analysis (**Figure 7D**) indicated that most proteins were involved in metabolic process 23%, signaling pathway 19%, biological regulation 17%, and infection 16%.

To further explore the mechanism of osteogenesis, we examined the expression levels of the BMP-Smads signaling pathway; western blot analysis showed that the expression levels of BMPR1A and BMPR2 and the phosphorylation levels of Smad4 and Smad1/5/8 in the hBMSCs BMP-Smads signaling pathway in the pTi-SMF group were significantly higher than those in the Ti group (**Figure 8A**), and the differences were statistically significant ($P=0.001$, $P<0.001$, $P=0.001$, $P=0.008$, **Figure 8B**) for these results. It can be inferred that the enhanced bone regeneration in the pTi-SMF group may be caused by activation of the BMP-Smads signaling pathway.

Discussion

Due to its excellent load-bearing properties, excellent biocompatibility and excellent corrosion resistance, titanium has been used to repair bone defects [8]. Rapid prototyping is able to design and manufacture customized titanium medical implants with excellent mechanical and biological properties, and its properties can adjust according to clinical needs. At present, a variety of 3D-printed pTi implants have been applied in clinical practice [20, 21]. However, the method to further improve the bone conduction and osteoinduction properties of titanium substrates is still a hot topic in clinical application. The results showed that polydopamine coating could improve the bone regeneration ability of a titanium scaffold. This method is simple and easy. A one-step reaction can not only change the surface properties of titanium alloy but also provide a stable coating for covalent immobilization of drugs and proteins [22]. Catecholamine enhances the binding stability between polydopamine and titanium scaffolds by covalent cross linking with metal complexes, thus enhancing cell adhesion and increasing the immobilization of serum adhesion proteins [23,

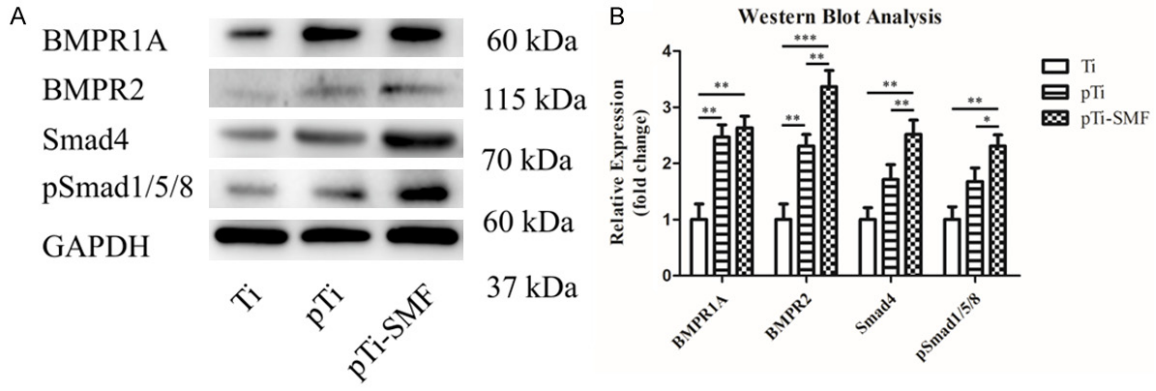

Figure 8. Western blot analysis of protein expression in the BMP-Smads signaling pathway in 3 groups of hBMSCs. A. The expression of BMPR1A, BMPR2, Smad4 and psmad1/5/8 in hBMSC determined by western blot after 14 days of culture. B. Quantitative analysis of western blot between 3 groups. The experiment was repeated for 3 times. *P<0.05, **P<0.01, ***P<0.001.

24]. Wet ability and roughness of the substrate surface are known to be two important factors in cell response to the substrate [25, 26] Costa *et al.* demonstrated that the surface morphology and roughness of the substrate improved cell adhesion and migration in osteoblasts [26]. The polydopamine coating can not only increase the surface roughness of titanium substrate but also decrease the water contact angle and improve the wetting ability of the titanium scaffold [27].

As for improving bone conduction and induction, in addition to changing the surface properties of implants, biophysical stimulation techniques can also promote bone regeneration, and they have many obvious advantages in clinical treatment. Recent studies have shown that SMF can enhance bone regeneration in scaffolds [28, 29]. SMF as an effective and noninvasive treatment has been shown to accelerate fracture healing, stimulate bone regeneration, promote osseointegration of implants and increase bone mineral density *in vivo* [30, 31]. A lack of naturally weak SMF can cause insomnia, fatigue and depression in humans and increase the risk of osteoporosis. Moderate SMF can enhance cartilage and bone regeneration by improving extracellular matrix formation [32, 33]. The application of a low-frequency magnetic field can reduce inflammation and degenerative changes in human osteoarthritis, and SMF can reduce pain and improve functional status in patients with rheumatoid arthritis in the range of 50 to 180 mT [34]. SMF of moderate intensity has been shown to promote new bone formation, prevent bone mineral density loss, and induce cartilage metabolic activity in humans and rodents [33]. Studies by Kotani *et al.* [35] have shown that strong SMF (8T) stimulates bone formation by increasing matrix formation and osteoblast differentiation, and it has been demonstrated for the first time that strong SMF can improve the formation of bone morphogenetic protein (BMP2) and surrounding ectopic bone by regulating the growth direction of osteoblasts (MC3T3-E1 cells). SMF affects the growth of bone and chondroblasts, thus providing a new treatment for fracture healing, SMF combined with effective factors affecting bone regeneration may be a promising approach in the field of bone regeneration medicine.

Although the effect of polydopamine coating and SMF on bone regeneration has been well known, research on polydopamine coating combined with static magnetic field to promote bone regeneration in the substrate has not been reported. We report for the first time that polydopamine as a drug-loading coating combined with static magnetic field can promote bone regeneration in the substrate. As a drug-loaded coating, polydopamine can carry drugs or particle materials to promote the proliferation and differentiation of bone cells by improving the surface properties of implants. SMF can promote bone regeneration *in vitro* and is non-invasive, safe and easy to use. Therefore, the combination of polydopamine coating and static magnetic field to enhance bone regeneration in 3D printed porous titanium scaffolds has

broad prospects in the clinical work of repairing bone defects.

The study of Paun IA *et al.* showed that the cells in a 3D superparamagnetic scaffold in the SMF-stimulated group showed more deformation, stronger cell mineralization, and faster bone regeneration than the unstimulated specimens [36]. And Studies by Steffi C *et al.* have shown that polydopamine coating can reduce osteoclast differentiation [37]. The results of the CCK-8 and LIVE/DEAD viability/cytotoxicity assays showed that polydopamine coating combined with static magnetic field (100 mT) could enhance the viability, proliferation and survival of hBMSCs in 3D printed porous titanium scaffolds. We hypothesized that the polydopamine coating increased the wettability and roughness of the titanium substrate and promoted the proliferation and differentiation of hBMSCs. It is known that hBMSCs can differentiate into osteoblasts through multiple pathways, including osteoblast progenitor cells and preosteoblasts, which is an important factor affecting bone regeneration [38]. Mature osteoblasts are characterized by mineralization of the ECM to form hydroxylapatite [39]. The expression levels of several osteogenic markers, including Col-1, ALP and Runx2, were detected by RT-PCR and western blots in cells cultured for 14 days. All of these markers were significantly elevated. In addition, ARS staining showed that polydopamine with SMF promoted the differentiation of hBMSCs into osteoblasts. ALP, a key osteoblast marker involved in the initiation of mineralization, was also increased.

In the process of bone regeneration, cell adhesion is a crucial step in the contact between cells and the surface of the substrate, which greatly affects the cell morphology and the ability of proliferation and differentiation [40]. Therefore, cell adhesion and subsequent growth are important indicators of whether a material can be used as a substitute for bone regeneration. In this study, F-actin, vinculin and DAPI were used to demonstrate that polydopamine combined with SMF can improve the morphology of hBMSCs and increase the adhesion of hBMSCs. Bone morphogenetic proteins (BMPs) belong to the super family of transforming growth factor (TGF-β) and play a critical role in bone development, bone growth, and fracture repair [41]. It is reported that BMPR1A fusion protein alleviates radiation-induced bone loss in mice by increased bone formation and reduced bone resorption [42]. In addition, the expression of BMP2 is reported to promote in vitro bone formation and in vivo ectopic osteogenesis [43]. Smad4 is a TGF-specific inducer and is thought to play an important role in bone metabolism by participating in the development and function of osteoclasts and osteoblasts [44, 45]. In the study of Hsieh *et al.*, BMP2 and Smad4 expression were increased in osteoporotic fracture mice, and BMP2 can regulate Smad4, which may help to induce osteoblast proliferation and differentiation, leading to osteogenesis [46]. In addition, BMP2 is a key signal transduction component in bone formation, which is mediated by Smad4, a nuclear transcription factor that regulates the activity of TGF-β ligand and plays an important role in bone formation [47]. If the BMP-Smads signaling pathway was damaged, the osteoblast differentiation will be inhibited [48].

In our study, we tried to improve osteogenesis capacity by modifying the scaffold surface. We found that the osteogenic ability of hBMSCs was significantly enhanced by exposured to the polydopamine coating and SMF. To illustrate the underlying mechanism, the proteomics was performed to identify the differential proteins. The results pointed out that the activated BMP-Smads signaling pathway was a key factor to explain the enhanced osteogenesis. Subsequently, we used western blot analysis to verify the activation of the signaling pathway. Based on these results, we investigated the expression level of the TGF/BMP-Smads signaling pathway (**Figure 8**) to further understand the mechanism of osteogenesis. The BMP-Smads pathway is composed of BMP signal, BMP receptor and receptor substrate Smad signal molecule [49]. BMP ligands act on membrane type II receptors, and the self-phosphorylation of the membrane leads to the activation of the type I receptor and subsequent phosphorylation. This form of heteropolymer complex, phosphorylated by Smad1, Smad5 and Smad8, transmits signals to cells [50, 51]. The activated R-Smad and Smad4 then bind in the cytoplasm to form the R-SMad/Smad4 complex, which transmits signals to the nucleus and binds to target genes, thereby activating transcription and signal transduction of target genes [52]. The present results showed

that the expression levels of BMPR2 and pSmad1/5/8 increased, suggesting that the BMP-Smad1/5/8 signaling pathway is associated with polydopamine with SMF exposure. The results showed that the distribution of Smad4 was concentrated in the nucleus after polydopamine with SMF treatment. Meanwhile, Smad4, Smad2/3 and Smad1/5/8 were found to be enriched in the cells, especially in the nucleus, according to the results of protein imprinting. This suggests that polydopamine combined with SMF can stimulate Smad4 to activate the BMP-Smad1/5/8 signaling pathway and increase intranuclear pR-Smads translocation to promote osteogenesis.

Conclusion

The results showed that polydopamine coating combined with static magnetic field could enhance the cell viability and proliferation of hBMSCs, improve the morphology of hBMSCs, enhance the adhesion of hBMSCs, and promote the osteogenic differentiation of hBMSCs. The mechanism occurs by upregulating the BMP-Smads signaling pathway.

Acknowledgements

L.K. and Y.H. contributed equally to this work. This article was supported by the Science and Technology Development Program of Shandong Province (No. 2015GSF118110). The authors thank AJE company (Durham, North Carolina, USA) for editing the English text of a draft of this manuscript.

Disclosure of conflict of interest

None.

Address correspondence to: Dr. Fu Wang, Department of Orthopaedics, Shandong Provincial Hospital Affiliated to Shandong First Medical University, No. 324, Jingwu Road, Jinan 250021, Shandong, P. R. China. E-mail: wangfu197286@163.com

References

[1] Qiao H and Tang TT. Engineering 3D approaches to model the dynamic microenvironments of cancer bone metastasis. Bone Res 2018; 6: 3.

[2] Shie MY, Chiang WH, Chen IWP, Liu WY and Chen YW. Synergistic acceleration in the osteogenic and angiogenic differentiation of human mesenchymal stem cells by calcium silicate-graphene composites. Mater Sci Eng C Mater Biol Appl 2017; 73: 726-735.

[3] Khademhosseini A and Langer R. A decade of progress in tissue engineering. Nat Protoc 2009; 300: 64-71.

[4] Chien CY and Tsai WB. Poly(dopamine)-assisted immobilization of Arg-Gly-Asp peptides, hydroxyapatite, and bone morphogenic protein-2 on titanium to improve the osteogenesis of bone marrow stem cells. ACS Appl Mater Interfaces 2013; 5: 6975-6983.

[5] Gaharwar AK, Mihaila SM, Swami A, Patel A, Sant S, Reis RL, Marques AP, Gomes ME and Khademhosseini A. Bioactive silicate nanoplatelets for osteogenic differentiation of human mesenchymal stem cells. Adv Mater 2013; 25: 3329-3336.

[6] Hollister SJ, Levy RA, Chu TM, Halloran JW and Feinberg SE. An image-based approach for designing and manufacturing craniofacial scaffolds. Int J Oral Maxillofac Surg 2000; 29: 67-71.

[7] Liu H, Li W, Liu C, Tan J, Wang H, Hai B, Cai H, Leng HJ, Liu ZJ and Song CL. Incorporating simvastatin/poloxamer 407 hydrogel into 3D-printed porous Ti6Al4V scaffolds for the promotion of angiogenesis, osseointegration and bone ingrowth. Biofabrication 2016; 8: 045012.

[8] Le Guéhennec L, Soueidan A, Layrolle P and Amouriq Y. Surface treatments of titanium dental implants for rapid osseointegration. Dent Mater 2007; 23: 844-854.

[9] Lai M, Cai K, Zhao L, Chen X, Hou Y and Yang Z. Surface functionalization of TiO2 nanotubes with bone morphogenetic protein 2 and its synergistic effect on the differentiation of mesenchymal stem cells. Biomacromolecules 2011; 12: 1097-1105.

[10] Lynge ME, van der Westen R, Postma A and Städler B. Polydopamine--a nature-inspired polymer coating for biomedical science. Nanoscale 2011; 3: 4916-4928.

[11] Xu M, Zhang Y, Zhai D, Chang J and Wu C. Mussel-inspired bioactive ceramics with improved bioactivity, cell proliferation, differentiation and bone-related gene expression of MC3T3 cells. Biomater Sci 2013; 1: 933-941.

[12] Wu C, Han P, Liu X, Xu M, Tian T, Chang J and Xiao Y. Mussel-inspired bioceramics with self-assembled Ca-P/polydopamine composite nanolayer: preparation, formation mechanism, improved cellular bioactivity and osteogenic differentiation of bone marrow stromal cells. Acta Biomater 2014; 10: 428-438.

[13] Miyakoshi J. Effects of static magnetic fields at the cellular level. Prog Biophys Mol Biol 2005; 87: 213-223.

[14] Wang Y and Qin QH. A theoretical study of bone remodelling under PEMF at cellular level. Comput Methods Biomech Biomed Engin 2011; 15: 885-897.
[15] Trock DH. Electromagnetic fields and magnets. Investigational treatment for musculoskeletal disorders. Rheum Dis Clin North Am 2000; 26: 51-62.
[16] Markov MS. Magnetic field therapy: a review. Electromagn Biol Med 2007; 26: 1-23.
[17] Reginster JY, Pelousse F and Bruyère O. Safety concerns with the long-term management of osteoporosis. Expert Opin Drug Saf 2013; 12: 507-522.
[18] Zhang J, Ding C, Ren L, Zhou Y and Shang P. The effects of static magnetic fields on bone. Prog Biophys Mol Biol 2013; 114: 146-152.
[19] He Y, Yu LJ, Liu JY, Li YQ, Wu YH, Huang ZF, Wu D, Wang H, Wu ZH and Qiu GX. Enhanced osteogenic differentiation of human bone-derived mesenchymal stem cells in 3-dimensional printed porous titanium scaffolds by static magnetic field through up-regulating Smad4. FASEB J 2019; 33: 6069-6081.
[20] Patel V, Kovalsky D, Meyer SC, Chowdhary A, Lockstadt H, Techy F, Billys J, Limoni R, Yuan PS, Kranenburg A, Cher D and Tender G. Minimally invasive lateral transiliac sacroiliac joint fusion using 3D-printed triangular titanium implants. Med Devices (Auckl) 2019; 12: 203-214.
[21] Sultan AA, Mahmood B, Samuel LT, Stearns KL, Molloy RM, Moskal JT, Krebs VE, Harwin SF and Mont MA. Cementless 3D printed highly porous titanium-coated baseplate total knee arthroplasty: survivorship and outcomes at 2-year minimum follow-up. J Knee Surg 2020; 33: 279-283.
[22] Wei Q, Achazi K, Liebe H, Schulz A, Noeske PL, Grunwald I and Haag R. Mussel-inspired dendritic polymers as universal multifunctional coatings. Angew Chem Int Ed Engl 2014; 53: 11650-11655.
[23] Tsai WB, Chen WT, Chien HW, Kuo WH and Wang MJ. Poly(dopamine) coating of scaffolds for articular cartilage tissue engineering. Acta Biomater 2011; 7: 4187-4194.
[24] Guo L, Liu Q, Li G, Shi J, Liu J, Wang T and Jiang G. A mussel-inspired polydopamine coating as a versatile platform for the in situ synthesis of graphene-based nanocomposites. Nanoscale 2012; 4: 5864-5867.
[25] Bayram C, Demirbilek M, Caliskan N, Demirbilek ME and Denkbas EB. Osteoblast activity on anodized titania nanotubes: effect of simulated body fluid soaking time. J Biomed Nanotechnol 2012; 8: 482-490.
[26] Costa DO, Prowse PD, Chrones T, Sims SM, Hamilton DW, Rizkalla AS and Dixon SJ. The differential regulation of osteoblast and osteoclast activity by surface topography of hydroxyapatite coatings. Biomaterials 2013; 34: 7215-7226.
[27] Huang Z, Wu Z, Ma B, Yu L, He Y, Xu D, Wu Y, Wang H and Qiu G. Enhanced biocompatibility and osteogenesis of titanium substrates immobilized with dopamine-assisted superparamagnetic Fe_3O_4 nanoparticles for hBMSCs. R Soc Open Sci 2018; 5: 172033.
[28] Xia Y, Chen H, Zhao Y, Zhang F, Li X, Wang L, Weir MD, Ma J, Reynolds MA, Gu N and Xu HHK. Novel magnetic calcium phosphate-stem cell construct with magnetic field enhances osteogenic differentiation and bone tissue engineering. Mater Sci Eng C Mater Biol Appl 2019; 98: 30-41.
[29] Huang Z, He Y, Chang X, Liu J, Yu L, Wu Y, Li Y, Tian J, Kang L, Wu D, Wang H, Wu Z and Qiu G. A magnetic iron oxide/polydopamine coating can improve osteogenesis of 3d-printed porous titanium scaffolds with a static magnetic field by upregulating the TGFβ-Smads pathway. Adv Healthc Mater 2020; 9: e2000318.
[30] Costantino C, Pogliacomi F, Passera F and Concari G. Treatment of wrist and hand fractures with natural magnets:preliminary report. Acta Biomed 2007; 78: 198-203.
[31] Aydin N and Bezer M. The effect of an intramedullary implant with a static magneticfield on the healing of the osteotomised rabbit femur. Int Orthop 2011; 35: 135-141.
[32] Meng J, Xiao B, Zhang Y, Liu J, Xue H, Lei J, Kong H, Huang Y, Jin Z, Gu N and Xu H. Superparamagnetic responsive nanofibrous scaffolds under static magnetic field enhance osteogenesis for bone repair in vivo. Sci Rep 2013; 3: 2655.
[33] Jaberi FM, Keshtgar S, Tavakkoli A, Pishva E, Geramizadeh B, Tanideh N and Jaberi MM. A moderate-intensity static magnetic field enhances repair of cartilage damage in rabbits. Arch Med Res 2011; 42: 268-273.
[34] Marycz K, Kornicka K and Röcken M. Static magnetic field (SMF) as a regulator of stem cell fate-new perspectives in regenerative medicine arising from an underestimated tool. Stem Cell Rev Rep 2018; 14: 785-792.
[35] Kotani H, Kawaguchi H, Shimoaka T, Iwasaka M, Ueno S, Ozawa H, Nakamura K and Hoshi K. Strong static magnetic field stimulates bone formation to a definite orientation in vitro and in vivo. J Bone Miner Res 2002; 17: 1814-1821.
[36] Paun IA, Calin BS, Mustaciosu CC, Mihailescu M, Moldovan A, Crisan O, Leca A and Luculescu CR. 3D superparamagnetic scaffolds for bone mineralization under static magnetic field stimulation. Materials 2019; 12: E2834.

[37] Steffi C, Shi Z, Kong CH and Wang W. Bioinspired polydopamine and polyphenol tannic acid functionalized titanium suppress osteoclast differentiation: a facile and efficient strategy to regulate osteoclast activity at bone-implant interface. J R Soc Interface 2019; 16: 20180799.
[38] Bianco P, Riminucci M, Gronthos S and Robey PG. Bone marrow stromal stem cells: nature, biology, and potential applications. Stem Cells 2001; 19: 180-192.
[39] Arvidson K, Abdallah BM, Applegate LA, Baldini N, Cenni E, Gomez-Barrena E, Granchi D, Kassem M, Konttinen YT, Mustafa K, Pioletti DP, Sillat T and Finne-Wistrand A. Bone regeneration and stem cells. J Cell Mol Med 2011; 15: 718-746.
[40] Ma Z, Kotaki M, Yong T, He W and Ramakrishna S. Surface engineering of electrospun polyethylene terephthalate (PET) nanofibers towards development of a new material for blood vessel engineering. Biomaterials 2005; 26: 2527-2536.
[41] Rosen V. BMP2 signaling in bone development and repair. Cytokine Growth Factor Rev 2009; 20: 475-480.
[42] Wang S, Li J, Sun H, Sha L, Guo Y, Gu G, Mao J, Nie X, Zhai Y, Yu D, Zhai J, Li H, Shan X, Dai C, Wu X, He X, Xin L, Liu J, Heng K and Geng Q. Treatment with soluble bone morphogenetic protein type 1A receptor fusion protein alleviates irradiation-induced bone loss in mice through increased bone formation and reduced bone resorption. Am J Transl Res 2020; 12: 743-757.
[43] Qiao C, Zhang K, Sun B, Liu J, Song J, Hu Y, Yang S, Sun H and Yang B. Sustained release poly (lactic-co-glycolic acid) microspheres of bone morphogenetic protein 2 plasmid/calcium phosphate to promote in vitro bone formation and in vivo ectopic osteogenesis. Am J Transl Res 2015; 7: 2561-2572.
[44] Kim BJ, Hwang JY, Han BG, Lee JY, Lee JY, Park EK, Lee SH, Chung YE, Kim GS, Kim SY and Koh JM. Association of SMAD2 polymorphisms with bone mineral density in postmenopausal Korean women. Osteoporosis Int 2011; 22: 2273-2282.
[45] Moon YJ, Yun CY, Choi H, Ka SO, Kim JR, Park BH and Cho ES. Smad4 controls bone homeostasis through regulation of osteoblast/osteocyte viability. Exp Mol Med 2016; 48: e256.
[46] Hsieh TP, Sheu SY, Sun JS, Chen MH and Liu MH. Icariin isolated from epimedium pubescens regulates osteoblasts anabolism through BMP-2, SMAD4, and Cbfa1 expression. Phytomedicine 2010; 17: 414-423.
[47] Liang W, Lin M, Li X, Li C, Gao B, Gan H, Yang Z, Lin X, Liao L and Yang M. Icariin promotes bone formation via the BMP-2/Smad4 signal transduction pathway in the hFOB 1.19 human osteoblastic cell line. Int J Mol Med 2012; 30: 889-895.
[48] Sun GJ, Yang SF, Ti YF, Guo GD, Fan GT, Chen FR, Xu SG and Zhao JN. Influence of ceramic debris on osteoblast behaviors: an in vivo study. Orthop Surg 2019; 11: 770-776.
[49] Edlund S, Landström M, Heldin CH and Aspenström P. Smad7 is required for TGF-beta-induced activation of the small GTPase Cdc42. J Cell Sci 2004; 117: 1835-1847.
[50] Chen G, Deng C and Li YP. TGF-β and BMP signaling in osteoblast differentiation and bone formation. Int J Biol Sci 2012; 8: 272-288.
[51] Konstantinidis G, Moustakas A and Stournaras C. Regulation of myosin light chain function by BMP signaling controls actin cytoskeleton remodeling. Cell Physiol Biochem 2011; 28: 1031-1044.
[52] Jun JH, Yoon WJ, Seo SB, Woo KM, Kim GS, Ryoo HM and Baek JH. BMP2-activated Erk/MAP kinase stabilizes Runx2 by increasing p300 levels and histone acetyltransferase activity. J Biol Chem 2010; 285: 36410-36419.

Table S1. The differential proteins between the pTi-SMF and Ti group

No.	Protein ID	Name	Score	Ratio (pTi-SMF/Ti)
1	Q92621	Nuclear pore complex protein Nup205	6.969	100.281
2	O00142	Thymidine kinase 2, mitochondrial	4.267	59.697
3	Q5T447	E3 ubiquitin-protein ligase HECTD3	1.964	58.356
4	Q9Y657	Spindlin-1	2.467	36.323
5	Q8IU81	Interferon regulatory factor 2-binding protein 1	4.852	12.498
6	Q8N543	Prolyl 3-hydroxylase OGFOD1	2.217	8.221
7	Q9UIV1	CCR4-NOT transcription complex subunit 7	1.889	7.547
8	Q96LD4	Gene overexpressed in astrocytoma protein	10.237	7.265
9	Q8ND90	Paraneoplastic antigen Ma1	2.158	5.982
10	O75330	Hyaluronan mediated motility receptor	1.923	5.924
11	Q9Y450	HBS1-like protein	9.011	5.492
12	P98175	RNA-binding protein 10	5.487	5.456
13	Q5BKU9	Oxidoreductase-like domain-containing protein 1	1.817	5.447
14	Q96KF7	Small integral membrane protein 8	1.986	5.379
15	O60346	PH domain leucine-rich repeat-containing protein phosphatase 1	2.251	5.239
16	Q6UW02	Cytochrome P450 20A1	17.863	5.078
17	Q5UCC4	ER membrane protein complex subunit 10	46.994	4.950
18	P15924	Desmoplakin	7.630	4.248
19	Q15643	Thyroid receptor-interacting protein 11	14.725	4.104
20	Q66K14	TBC1 domain family member 9B	3.166	3.931
21	O60879	Protein diaphanous homolog 2	7.436	3.718
22	O95721	Synaptosomal-associated protein 29	25.040	3.713
23	Q9UBU9	Nuclear RNA export factor 1	5.963	3.578
24	P50583	Bis(5'-nucleosyl)-tetraphosphatase	3.206	3.560
25	Q8N4P3	Guanosine-3',5'-bis(diphosphate) 3'-pyrophosphohydrolase MESH1	13.806	3.506
26	P14621	Acylphosphatase-2	4.305	3.500
27	O43148	mRNA cap guanine-N7 methyltransferase	7.125	3.491
28	O76024	Wolframin	3.949	3.345
29	Q01415	N-acetylgalactosamine kinase	2.529	3.279
30	Q6PIU2	Neutral cholesterol ester hydrolase 1	5.048	3.212
31	Q96EP0	E3 ubiquitin-protein ligase RNF31	3.712	3.155
32	Q96AQ6	Pre-B-cell leukemia transcription factor-interacting protein 1	3.617	3.044
33	Q9H7D7	WD repeat-containing protein 26	6.444	2.997
34	O94992	Protein HEXIM1	8.621	2.958
35	Q9NV70	Exocyst complex component 1	20.588	2.952
36	P61923	Coatomer subunit zeta-1	23.259	2.809
37	Q5BJD5	Transmembrane protein 41B	6.202	2.789
38	Q9NPA0	ER membrane protein complex subunit 7	2.735	2.682
39	Q8N128	Protein FAM177A1	4.928	2.678
40	Q3YEC7	Rab-like protein 6	4.965	2.637
41	Q9UMS6	Synaptopodin-2	2.385	2.610
42	O75400	Pre-mRNA-processing factor 40 homolog A	8.867	2.571
43	Q9NWZ3	Interleukin-1 receptor-associated kinase 4	2.616	2.529
44	O15455	Toll-like receptor 3	2.371	2.526
45	O75688	Protein phosphatase 1B	3.346	2.514
46	Q96C01	Protein FAM136A	3.932	2.481
47	Q9Y217	Myotubularin-related protein 6	2.810	2.466
48	Q08170	Serine/arginine-rich splicing factor 4	2.814	2.438
49	Q5SRE7	Phytanoyl-CoA dioxygenase domain-containing protein 1	6.009	2.419
50	Q8NEY8	Periphilin-1	3.591	2.404

51	P35249	Replication factor C subunit 4	2.712	2.390
52	Q9NPH2	Inositol-3-phosphate synthase 1	5.911	2.388
53	Q6ZUX7	LHFPL tetraspan subfamily member 2 protein	11.065	2.377
54	P17936	Insulin-like growth factor-binding protein 3	9.204	2.368
55	O75475	PC4 and SFRS1-interacting protein	10.396	2.304
56	Q6PJG2	Mitotic deacetylase-associated SANT domain protein	4.661	2.299
57	Q14137	Ribosome biogenesis protein BOP1	7.643	2.286
58	Q53GS9	U4/U6.U5 tri-snRNP-associated protein 2	3.324	2.284
59	O60437	Periplakin	102.550	2.262
60	P43007	Neutral amino acid transporter A	4.226	2.225
61	Q9H3M7	Thioredoxin-interacting protein	3.762	2.220
62	O95967	EGF-containing fibulin-like extracellular matrix protein 2	4.188	2.200
63	Q5SWX8	Protein odr-4 homolog	2.081	2.194
64	O15230	Laminin subunit alpha-5	9.803	2.189
65	Q9BXW7	Haloacid dehalogenase-like hydrolase domain-containing 5	18.642	2.186
66	Q92934	Bcl2-associated agonist of cell death	6.487	2.172
67	Q15036	Sorting nexin-17	6.064	2.134
68	Q7Z2Z1	Treslin	2.267	2.134
69	O43741	5'-AMP-activated protein kinase subunit beta-2	4.442	2.129
70	Q9UI15	Transgelin-3	2.163	2.076
71	Q13485	Mothers against decapentaplegic homolog 4	2.035	2.067
72	A8MXV4	Nucleoside diphosphate-linked moiety X motif 19	2.809	2.049
73	P21397	Amine oxidase [flavin-containing] A	34.046	2.045
74	P36915	Guanine nucleotide-binding protein-like 1	11.896	2.039
75	Q9Y676	28S ribosomal protein S18b, mitochondrial	7.978	2.025
76	Q86WR0	Coiled-coil domain-containing protein 25	9.136	2.016
77	Q9UI09	NADH dehydrogenase 1 alpha subcomplex subunit 12	14.186	2.014
78	Q7Z6K5	Arpin	4.947	0.494
79	Q6UW68	Transmembrane protein 205	18.192	0.490
80	B1ANS9	WD repeat-containing protein 64	2.755	0.485
81	P60953	Cell division control protein 42 homolog	33.385	0.485
82	Q9NZD2	Glycolipid transfer protein	3.197	0.484
83	O75462	Cytokine receptor-like factor 1	11.732	0.484
84	P11802	Cyclin-dependent kinase 4	11.279	0.478
85	P56537	Eukaryotic translation initiation factor 6	140.750	0.476
86	Q9NQ50	39S ribosomal protein L40, mitochondrial	15.743	0.473
87	Q9Y3B7	39S ribosomal protein L11, mitochondrial	17.514	0.469
88	P51888	Prolargin	56.723	0.468
89	Q9BQS8	FYVE and coiled-coil domain-containing protein 1	50.004	0.465
90	O75122	CLIP-associating protein 2	3.104	0.465
91	Q96HJ9	Protein FMC1 homolog	3.015	0.461
92	Q92990	Glomulin	3.765	0.458
93	Q9BQ61	Telomerase RNA component interacting RNase	4.512	0.456
94	Q9HC36	rRNA methyltransferase 3, mitochondrial	2.066	0.454
95	Q14657	EKC/KEOPS complex subunit LAGE3	3.410	0.449
96	Q8NFF5	FAD synthase	4.552	0.438
97	Q8WXI9	Transcriptional repressor p66-beta	7.970	0.430
98	Q8TCT8	Signal peptide peptidase-like 2A	2.857	0.430
99	P04264	Keratin, type II cytoskeletal 1	323.310	0.430
100	Q8WW22	DnaJ homolog subfamily A member 4	2.225	0.428
101	P29279	CCN family member 2	15.372	0.428
102	Q5SRE5	Nucleoporin NUP188 homolog	1.787	0.425

103	Q9UID3	Vacuolar protein sorting-associated protein 51 homolog	3.094	0.424
104	Q01130	Serine/arginine-rich splicing factor 2	60.274	0.406
105	Q96GX9	Methylthioribulose-1-phosphate dehydratase	2.711	0.406
106	Q8N6M0	Deubiquitinase OTUD6B	2.467	0.394
107	Q9BRZ2	E3 ubiquitin-protein ligase TRIM56	19.457	0.393
108	Q8IWL3	Iron-sulfur cluster co-chaperone protein HscB	7.917	0.392
109	Q8TEA7	TBC domain-containing protein kinase-like protein	2.343	0.390
110	Q9UHI8	A disintegrin and metalloproteinase with thrombospondin motifs 1	2.493	0.387
111	Q9Y3L5	Ras-related protein Rap-2c	4.536	0.386
112	Q9BX66	Sorbin and SH3 domain-containing protein 1	5.302	0.373
113	Q8IX30	Signal peptide, CUB and EGF-like domain-containing protein 3	15.688	0.369
114	Q5VW32	BRO1 domain-containing protein BROX	2.026	0.351
115	P85037	Forkhead box protein K1	6.403	0.351
116	Q16832	Discoidin domain-containing receptor 2	7.376	0.339
117	Q8TBP5	Membrane protein FAM174A	2.804	0.335
118	Q9UNX3	60S ribosomal protein L26-like 1	4.419	0.328
119	Q96PE2	Rho guanine nucleotide exchange factor 17	6.298	0.322
120	Q9Y221	60S ribosome subunit biogenesis protein NIP7 homolog	4.630	0.317
121	P60604	Ubiquitin-conjugating enzyme E2 G2	11.047	0.314
122	Q9NNW7	Thioredoxin reductase 2, mitochondrial	17.901	0.312
123	P11279	Lysosome-associated membrane glycoprotein 1	16.595	0.299
124	Q5VT52	Regulation of nuclear pre-mRNA domain-containing protein 2	3.137	0.282
125	O14613	Cdc42 effector protein 2	3.842	0.268
126	Q8NCC3	Group XV phospholipase A2	10.008	0.261
127	P84103	Serine/arginine-rich splicing factor 3	2.196	0.257
128	P00742	Coagulation factor X	8.682	0.252
129	Q6UWP8	Suprabasin	6.192	0.241
130	Q9UK41	Vacuolar protein sorting-associated protein 28 homolog	16.072	0.200
131	Q9BXR0	Queuine tRNA-ribosyltransferase catalytic subunit 1	16.225	0.197
132	Q9HCU5	Prolactin regulatory element-binding protein	5.010	0.193
133	Q9BYD1	39S ribosomal protein L13, mitochondrial	8.288	0.184
134	Q9Y5A7	NEDD8 ultimate buster 1	4.767	0.174
135	Q8N129	Protein canopy homolog 4	16.428	0.139
136	Q96BR5	Cytochrome c oxidase assembly factor 7	2.939	0.137
137	Q9C0D5	Protein TANC1	4.957	0.127
138	Q9H3S7	Tyrosine-protein phosphatase non-receptor type 23	27.052	0.114
139	Q96KP1	Exocyst complex component 2	9.766	0.100
140	Q5QJ74	Tubulin-specific chaperone cofactor E-like protein	7.827	0.099
141	Q9GZM5	Protein YIPF3	5.202	0.079
142	Q86W42	THO complex subunit 6 homolog	2.472	0.033
143	Q658P3	Metalloreductase STEAP3	2.474	0.031
144	Q6P1K8	General transcription factor IIH subunit 2-like protein	4.584	0.031
145	Q9NZR1	Tropomodulin-2	2.707	0.029
146	Q96EL3	39S ribosomal protein L53, mitochondrial	4.008	0.014
147	Q9BTE1	Dynactin subunit 5	4.352	0.004